Geoscience BC

Trace-Element Mapping by Laser Ablation–Inductively Coupled Plasma–Mass Spectrometry of Sulphide Minerals from the Burgundy Ridge Copper-Gold Alkalic Porphyry Prospect in the Golden Triangle, Northwestern British Columbia (NTS 104B/14E)

J. Dlugosz[1], Department of Earth, Environmental and Geographic Sciences, The University of British Columbia, Kelowna, British Columbia, joanna.dlugosz@ubc.ca

K.P. Larson, Department of Earth, Environmental and Geographic Sciences, The University of British Columbia, Kelowna, British Columbia

C.J.M Lawley, Natural Resources Canada, Geological Survey of Canada–Central, Ottawa, Ontario

C.J. Beno, Department of Earth, Environmental and Geographic Sciences, The University of British Columbia, Kelowna, British Columbia

D.C. Petts, Natural Resources Canada, Geological Survey of Canada–Central, Ottawa, Ontario

Introduction

Producing and advancing green technologies has become a topic of major interest in recent years due to the growing impact of humans on the environment. The geological materials that are susceptible to supply disruptions but are necessary for the production of these technologies have become known as 'critical minerals'. Demand for critical minerals in manufacturing of consumer (e.g., smartphones, electric vehicles) and commercial (e.g., in healthcare and construction of green infrastructure) products continues to grow and is estimated to increase six-fold within the next 17 years (Government of Canada, 2022). To meet such demands, federal and provincial governments are investing in programs centred around the research and exploration for critical mineral deposits.

One such program is the Targeted Geoscience Initiative, which was established in 2000 by the Government of Canada. This program has funded and carried out studies in all provinces and territories, including projects focused on the Golden Triangle of northwestern British Columbia (BC; Figure 1). The Golden Triangle has attracted both the mineral exploration industry and researchers due to its gold and critical-mineral endowment, and the resulting abundance of ore deposits.

The Burgundy Ridge prospect is a silica-undersaturated copper-gold alkalic porphyry deposit on the Newmont Lake property, owned by Enduro Metals Corp., located in the Golden Triangle between well-known deposits at Galore Creek, 30 km northwest, and Eskay Creek, 30 km southeast (Figures 1, 2). Active exploration has occurred on the property only within the last approximately 5 years and, as such, there is a lack of geological information concerning the prospect's petrogenesis and mineralization. Given the dearth of knowledge about the Burgundy Ridge prospect, The University of British Columbia, Okanagan, has partnered with Enduro Metals and the Geological Survey of Canada to begin characterizing the prospect in detail. Initial investigations have been focused on determining the timing of mineralization through rubidium-strontium geochronology, pyrite and chalcopyrite sulphur isotopes, and examination of trace elements within pyrite and chalcopyrite via micrometre-scale trace-element maps.

This paper presents the initial results and interpretations obtained from the laser ablation–inductively coupled plasma–mass spectrometry (LA-ICP-MS) chalcopyrite and pyrite trace-element maps. Such maps can be used to determine where critical minerals are hosted, as well as their abundances, and can inform interpretations about the conditions and origin of mineralization.

Geological Background

The western margin of Laurentia (the North American craton) has been tectonically active since the Late Precambrian (Nelson and Colpron, 2007), culminating in the for-
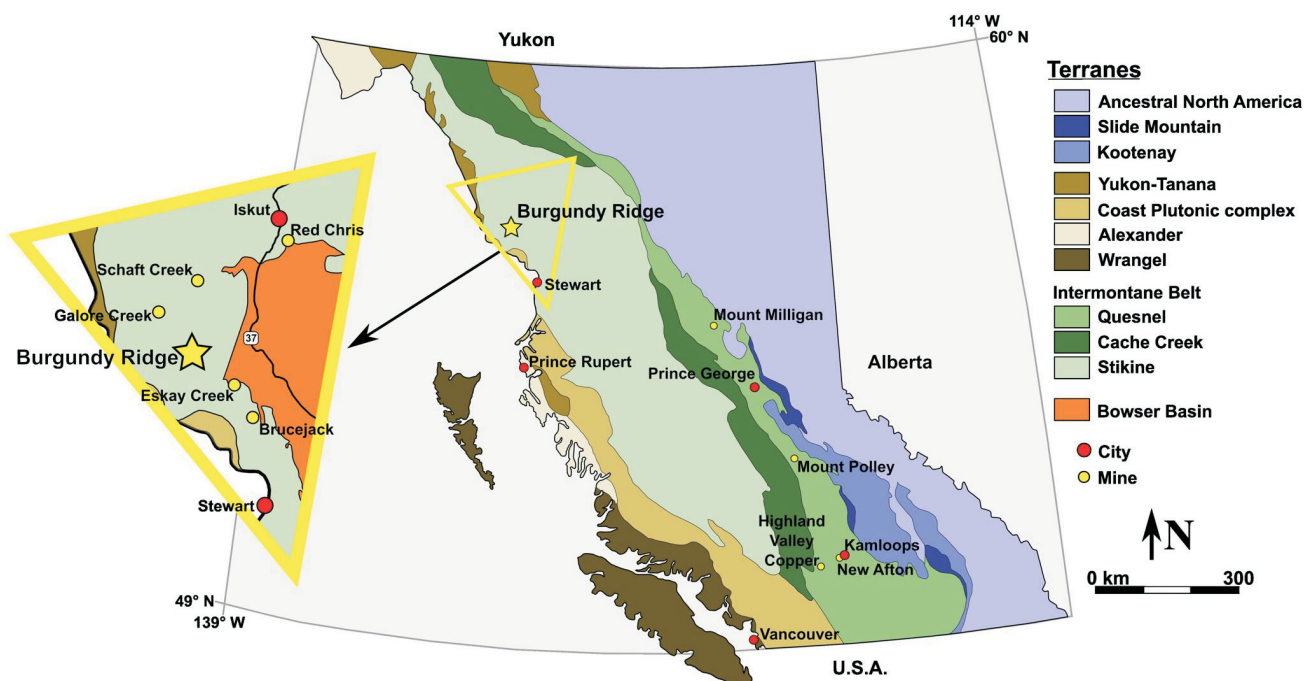
Figure 1. Terranes of British Columbia, the yellow triangle encompassing the area known as the 'Golden Triangle'. The Bowser Basin is incorporated into the Golden Triangle map since it is the largest depocentre covering this part of the Stikine terrane (Logan and Mihalynuk, 2014). Modified from del Real et al. (2013) and BC Geological Survey (2015, 2018).

mation of the Canadian Cordillera. In BC, the Canadian Cordillera is dominated by a series of oceanic basin and island-arc terranes that were accreted during the early Mesozoic to early Cenozoic (Coney et al., 1980; Dickinson, 2004; Nelson and Colpron, 2007; Logan and Mihalynuk, 2014). The terranes were brought in contact with the Laurentian margin due to subduction and the westward movement of Laurentia that closed intervening basins (Nelson and Colpron, 2007; Logan and Mihalynuk, 2014; Monger and Gibson, 2019). The accretion process deformed rocks deposited on the western margin of the North American craton and displaced them eastward. Active tectonism along the western portion of the Cordillera post-accretion resulted in pluton emplacement, volcanism, orogen-parallel dismemberment and variable metamorphism (Nelson and Colpron, 2007; Logan and Mihalynuk, 2014; Tombe, 2020).

The Intermontane belt, one of five tectonometamorphic belts that constitute the Cordillera in BC, includes the Stikine, Quesnel and Cache Creek terranes (Figure 1; Nelson and Colpron, 2007; Tombe, 2020). The Stikine and Quesnel terranes consist of volcanosedimentary sequences produced by pre-accretion Devonian to Early Jurassic arc magmatism and further post-accretion continental-arc magmatism in the late Early Jurassic (Logan and Mihalynuk, 2014). Accretion of these terranes to the North American craton occurred around 180 Ma, with the Cache Creek terrane (oceanic affinity) becoming wedged between the Stikine and Quesnel terranes (Nelson and Colpron, 2007; Logan and Mihalynuk, 2014).

Much of the mineral wealth in BC is contained within porphyry deposits of the Stikine and Quesnel terranes (Logan and Mihalynuk, 2014). Many of the porphyry deposits within these two terranes formed during the late Triassic to Early Jurassic, with significant mineralization occurring during a 6 m.y. pulse between 202 and 208 Ma (Lang et al., 1995; Logan and Mihalynuk, 2014). The porphyry deposits can be subdivided into two main groups: calcalkaline and alkaline (Lang et al., 1995; Logan and Mihalynuk, 2014). Calcalkaline porphyry deposits are more abundant globally (Lang et al., 1995) and are almost twice as common in BC, with 904 known occurrences (Logan and Mihalynuk, 2014). Alkaline deposits are less common in BC, with 431 known occurences, and globally, but are of interest because they can host economically significant amounts of copper, gold and other critical minerals (Deyell and Tosdal, 2005; Logan and Mihalynuk, 2014).

Alkalic porphyry deposits occur within the Golden Triangle of northwestern BC (Figure 1) in the Stikine terrane (Lang et al., 1995; Tombe, 2020), including one of the largest known alkalic porphyry deposits, Galore Creek (Micko, 2010; Tombe, 2020). The abundance of alkalic porphyries with economic potential in the Golden Triangle area provides an opportunity to enhance the understanding of these less-studied deposit types.

Methods

Samples from the Burgundy Ridge prospect were collected from core drilled during the 2019 and 2021 seasons at the

Newmont Lake property (Figure 2). Alteration assemblages and sulphide mineralogy and textures were documented in thin sections using a petrographic microscope (Figure 3). Areas for further investigation were selected from each sample to include different sulphide textures, including mineral shape and inclusion density. Focus was placed on sulphides because critical minerals are found primarily in sulphide crystal structures or around sulphide grains. Areas with multiple sulphide minerals, such as pyrite, chalcopyrite and sphalerite, were targeted to determine what critical minerals were hosted in which sulphide. Rock types with high levels of chalcopyrite and pyrite mineralization were focused on, resulting in three samples being selected from hydrothermal-breccia zones, since these are interpreted as forming during the main mineralization event (Figure 3).

Three trace-element maps of representative portions of chalcopyrite and pyrite grains were obtained through in situ LA-ICP-MS analysis in May 2023 at the Geological Survey of Canada in Ottawa, Ontario. Polished thick sections

(100 µm) from samples 138.4, 212.4 and 212.7 were mapped using an Agilent 7700x quadrupole ICP-MS instrument coupled to a Photon Machines Analyte G2 193 nm excimer laser-ablation system (Cabri and Jackson, 2011). Data acquisition was separated into two runs. Each analytical run was calibrated with a doped synthetic basalt glass standard GSE-1G (Guillong et al., 2005) and synthetic sulphide standards (Po689, Po726). The NIST610 glass-reference material was analyzed as a secondary reference material to quantify accuracy and precision. Reference materials were analyzed at the start and end of each run and bracketing every 20 mapping lines. A circular laser spot with a diameter of 10 µm was used during the analysis of sample 212.7, whereas a smaller spot diameter of 8 µm was used for samples 138.4 and 212.4. Prior to the main ablation, the target surfaces were rastered to clear away any surficial adherents. Both analytical runs used a laser repetition rate of 20 Hz and fluence of 4.5 J/cm^2.

Trace-element concentrations are reported in parts per million (ppm), whereas major elements expressed as oxides
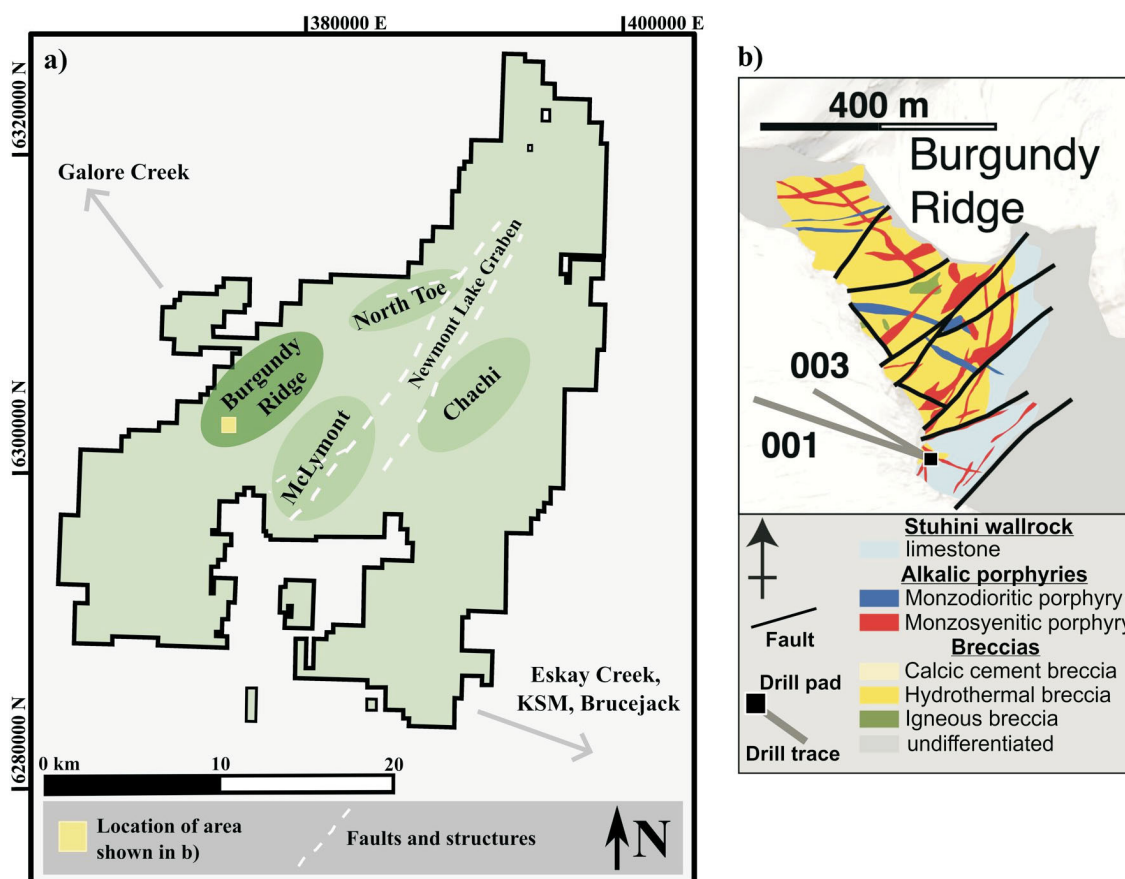

Figure 2. a) Enduro Metals Corp. Newmont Lake property and its prospects: Burgundy Ridge copper-gold porphyry, North Toe copper-gold porphyry, McLymont gold system and Chachi copper-gold-molybdenum anomaly. The prospects are hosted in the Golden Triangle of the Stikine terrane. The Galore Creek deposit is located 30 km northwest of the property, while the Eskay Creek past-producing mine, KSM deposit and Brucejack mine are all 30–50 km to the southeast. White dashed lines correspond to structural features on the property associated with the Newmont Lake graben. The yellow box represents the area shown in (b). **b)** Simplified map of the Burgundy Ridge prospect. Samples for trace-element maps were taken from drillholes 001 and 003. Modified from Ray et al. (1990) and Enduro Metals Corp. (2022, 2023).

are reported in weight percent (wt. %). Elements analyzed were ^{13}C, [34]S, [45]Sc, [47]Ti, [51]V, [53]Cr, [55]Mn, [57]Fe, [59]Co, [60]Ni, [65]Cu, [66]Zn, [75]As, [77]Se, [85]Rb, [88]Sr, [89]Y, [90]Zr, [95]Mo, [105]Pd, [108]Pd, [109]Ag, [111]Cd, [118]Sn, [121]Sb, [125]Te, [137]Ba, [140]Ce, [157]Gd, [173]Yb, [178]Hf, [181]Ta, [182]W, [185]Re, [195]Pt, [197]Au, [205]Tl, [206]Pb, [207]Pb, [208]Pb, [209]Bi and [238]U. Major elements reported as oxides were Na_2O, MgO, Al_2O_3, SiO_2, P_2O_5, K_2O, and CaO.

To create the maps, raw LA-ICP-MS files were processed within the open-source R software (R Development Core Team, 2018) using the LAMTRACE data-reduction approach outlined in Jackson (2008). Data processing fol-lowed the procedure outlined in Lawley et al. (2020) and included steps such as signal selection, background subtraction and conversion from continuous line scans to pixels to create the maps.

Further processing of the data from the trace-element maps was used to differentiate quantitative data from zones of differing compositions. Processing followed the methods outlined in Lawley et al. (2020) and utilized machine learning (R Development Core Team, 2018) in combination with multiple R packages such as robCompositions (Templ et al., 2011). First, to reduce problems when calculating a
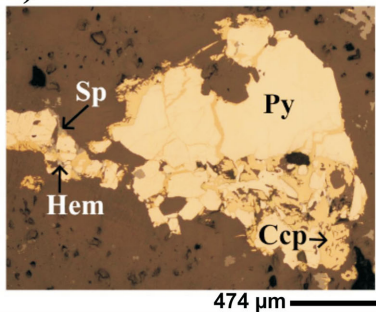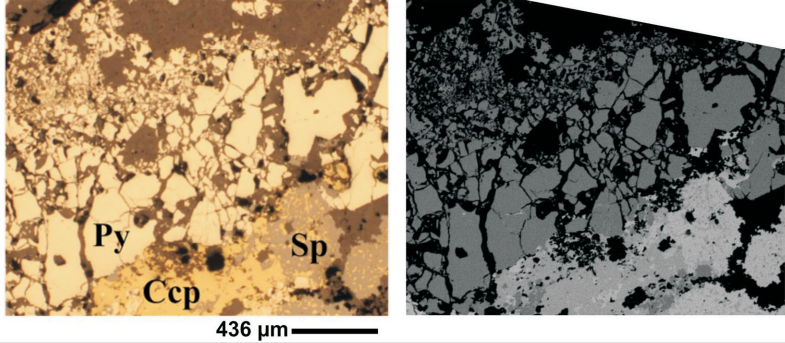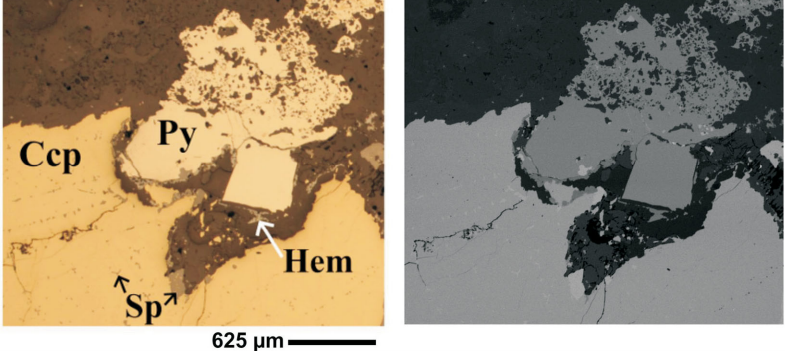
	Description
a) 138.4 	Hydrothermal breccia intruding Sparse Megacrystic Syenite zone Sulphides: pyrite (Py), chalcopyrite (Ccp), sphalerite (Sp) Alteration: chlorite, carbonate, sericite, hematite (Hem)
b) 212.4 	Cement-dominant hydrothermal breccia intruding Limestone zone Sulphides: pyrite (Py), chalcopyrite (Ccp), sphalerite (Sp) Alteration: K-feldspar, biotite, sericite, hematite
c) 212.7 	Hydrothermal breccia within a Biotite-Syenite zone Sulphides: pyrite (Py), chalcopyrite (Ccp), sphalerite (Sp) Alteration: K-feldspar, biotite, sericite, calcite, hematite (Hem)

Figure 3. Rock descriptions and identification of sulphides for samples **a)** 138.4, **b)** 212.4 and **c)** 212.7. Reflected-light images (left) and backscattered-electron images (right) were taken of the areas selected for LA-ICP-MS trace-element mapping. Brown areas in the re-flected light images are silicate minerals. Sample number is based on the depth, in metres, of each sample. Samples 138.4 and 212.7 are from drillhole 001, while sample 212.4 is from drillhole 003. Drillhole locations in the Burgundy Ridge prospect are shown in Figure 2b.

covariance matrix, elements with large portions of missing values (due to detection limits) within the dataset were filtered out. Next, a reduction of variables was accomplished through principal-component analysis. With these analyses, the initial principal components relate to elements with the largest variance. Clusters of principal-component scores from biplots are due to variations in chemical compositions based on mineral content or zonation within minerals. The number of these clusters is subjective and changes for each map, depending on the complexity of the minerals within the sample. The resulting cluster maps were used, along with reflected-light photos of the mapped areas, to name clusters based on the corresponding mineral, primarily focusing on sulphide mineralization, and whether the zones were core or rim domains. Distinguishing between different minerals, and different zones within minerals, allows for further interpretations to be made from trace-element maps, such as which mineral phases are more likely to host critical minerals and when these critical minerals became enriched in the hydrothermal history.

Results

Pyrite Trace-Element Results

Zones within pyrite crystals from all three samples are distinguishable based on variations in trace-element concentrations (Figures 4, 5, 6). Pyrite grains are typically characterized by Co-, Ni-, Bi- and As-poor cores, and enrichment of these same elements in the rims. The rim and core domains within pyrite were determined by the presence or absence of trace elements (Figures 4, 5, 6). Core domains for all three samples had a more defined euhedral shape, whereas the rim domains were more anhedral (Figures 4, 5, 6). The elements Se and Te are depleted in the most central regions of the pyrite cores, increase toward the outer regions and yield homogeneous concentrations across rims (Figures 4, 5, 6). Gold and As typically occur in the matrix between, or fractures within, pyrite grains, with some mineralization also occurring within late pyrite rims in samples 138.4 and 212.7 (Figures 4, 6). In sample 212.4, blebs of Pt occur in the inclusion-rich pyrite rims (Figure 5). These Pt blebs are spatially associated with areas of high As and Co concentrations.

Tellurium and Bi, which are considered critical minerals, and Au are found primarily in pyrite in the three samples. Of the three samples, sample 138.4 yielded the lowest average concentrations of Au and Bi (0.18 and 0.85 ppm respectively) and an average concentration of 13 ppm for Te (Figure 4). Sample 212.4 returned average concentrations of 0.89 ppm Au, 2.6 ppm Bi and 17 ppm Te (Figure 5). Lastly, average concentrations from sample 212.7 were 0.32 ppm Au, 3.4 ppm Bi and 12 ppm Te (Figure 6).

Pyrite was found to be more enriched in Co (average of 2439 ppm) compared to chalcopyrite (average 170 ppm)

across the three samples. Pyrite from sample 138.4 returned lower average Co concentrations than from the other two samples, with core concentrations at approximately 1500 ppm and rim concentrations at 1330 ppm (Figure 4). Pyrite rims in samples 212.4 and 212.7 shared similar average Co concentrations of 3450 and 3432 ppm, respectively. Cobalt concentrations in the cores of these pyrite grains showed more variation, with samples 212.7 and 212.4 containing Co concentrations of 264 ppm and 1735 ppm, respectively (Figures 5, 6).

Sample 212.7 returned the highest average Ni concentration of 1367 ppm (Figure 6). The majority of Ni was hosted within the pyrite rims of this sample, with an average concentration of 1728 ppm compared to an average concentration of 12 ppm for the core domain (Figure 6). Sample 212.4 contained the second highest concentration, although average concentration was considerably less (252 ppm) compared to sample 212.7 (Figure 5). Pyrite associated with chalcopyrite mineralization contained an average Ni concentration of 529 ppm, whereas inclusion-rich pyrite rims returned an average concentration of 135 ppm and cores returned the lowest concentration of 62 ppm (Figure 5). Sample 138.4 returned an overall average Ni concentration of 205 ppm, more similar to sample 212.4 than 212.7 (Figure 4). Pyrite cores within sample 138.4 continued the trend of Ni poor cores, with an average concentration of 114 ppm compared to the rim-zone concentration of 282 ppm (Figure 4).

Chalcopyrite Trace-Element Results

Chalcopyrite hosts the majority of Ag in the specimens analyzed, with samples 212.4 and 212.7 displaying a further enrichment of Ag along fractures within the chalcopyrite and at crystal boundaries (Figures 5, 6). In sample 138.4, both Ag and chalcopyrite occur in fractures within pyrite grains and immediately surrounding the grains (Figures 3a, 4). Concentration of Ag in chalcopyrite was the highest in sample 212.4 at 590 ppm, whereas samples 138.4 and 212.7 yielded 300 and 260 ppm, respectively.

Discussion

The trace-element maps outline multiple phases of pyrite mineralization, as defined by distinct changes in the concentration of elements from core and rim domains (Figure 4, 5, 6). Early pyrite cores are characterized by a general lack of Co, Ni, Te, Bi and As, whereas the same elements are enriched in rim domains. Moreover, Co concentrations oscillate in pyrite rim domains, most clearly seen in sample 212.7 (Figure 6), perhaps reflecting fluctuations in the composition of hydrothermal fluids responsible for sulphide precipitation or the kinetics of pyrite crystallization. Late, inclusion-rich pyrite, which is present in samples 212.4 (Figure 5) and 212.7 (Figure 6), is associated with
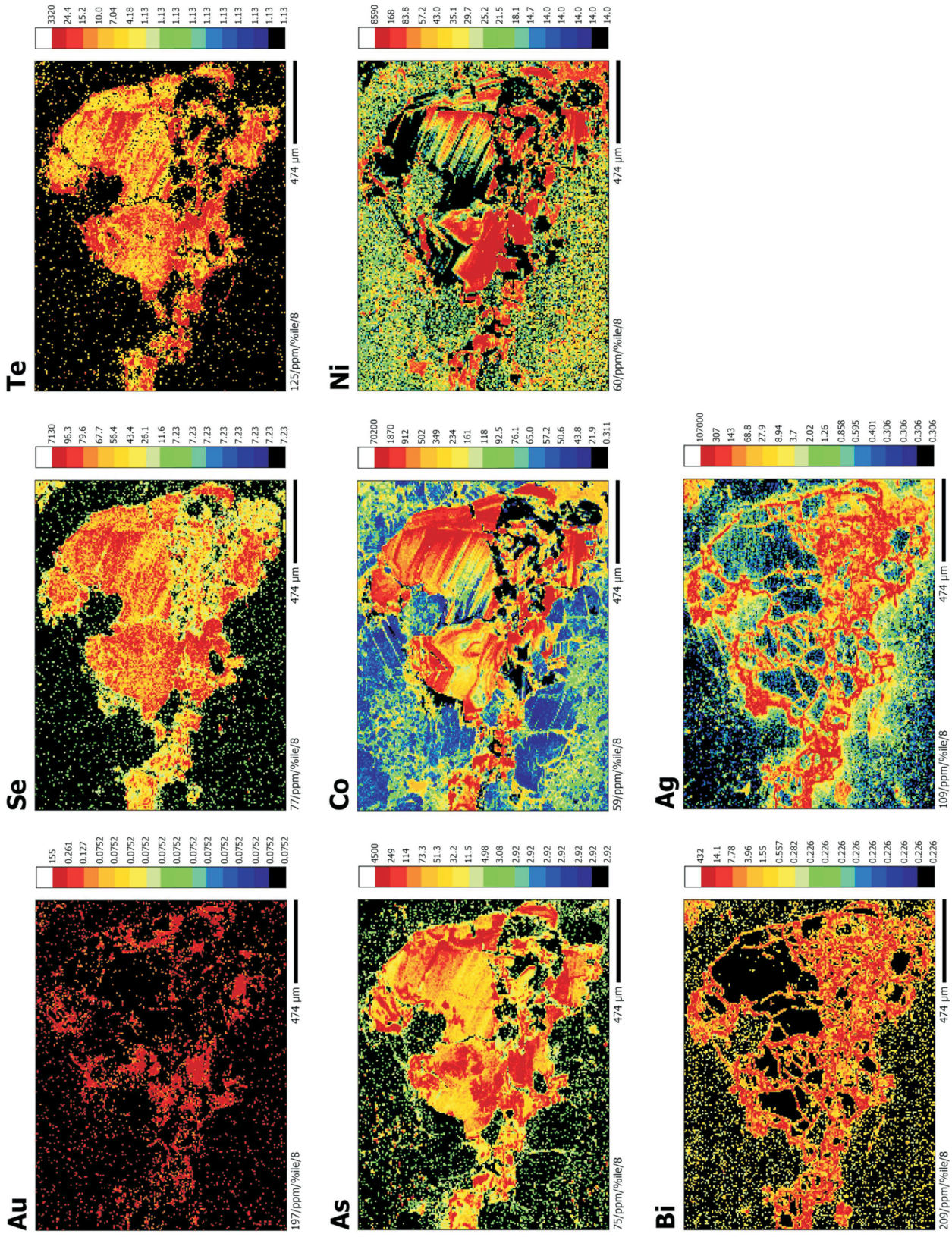
Figure 4. LA-ICP-MS trace-element maps of ^{197}Au, ^{77}Se, ^{125}Te, ^{75}As, ^{59}Co, ^{60}Ni, ^{209}Bi and ^{109}Ag in sulphide minerals from sample 138.4. Concentrations are in ppm.
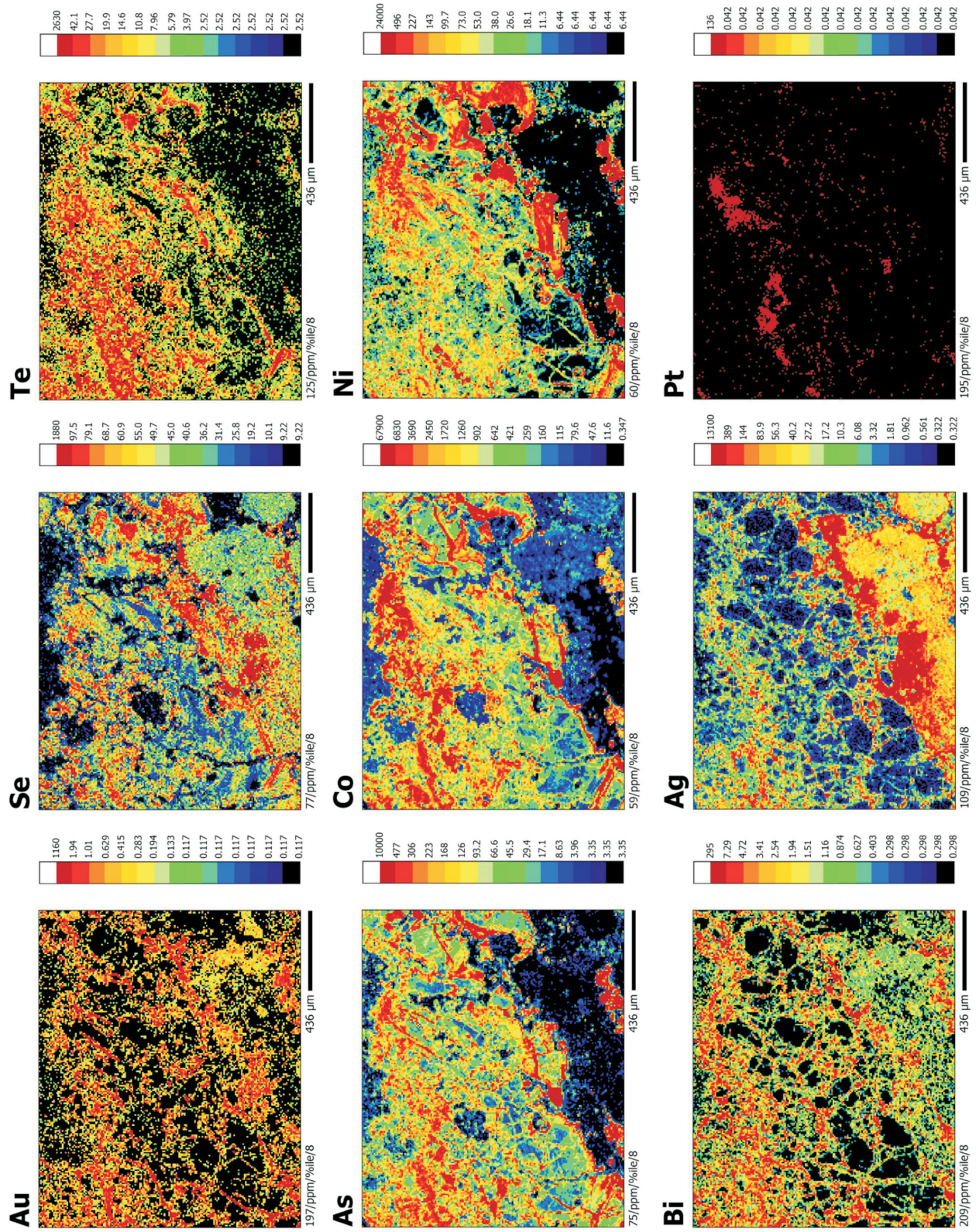
Figure 5. LA-ICP-MS trace-element maps of ^{197}Au, ^{77}Se, ^{125}Te, ^{75}As, ^{59}Co, ^{60}Ni, ^{209}Bi, ^{109}Ag and ^{195}Pt in sulphide minerals from sample 212.4. Concentrations are in ppm.
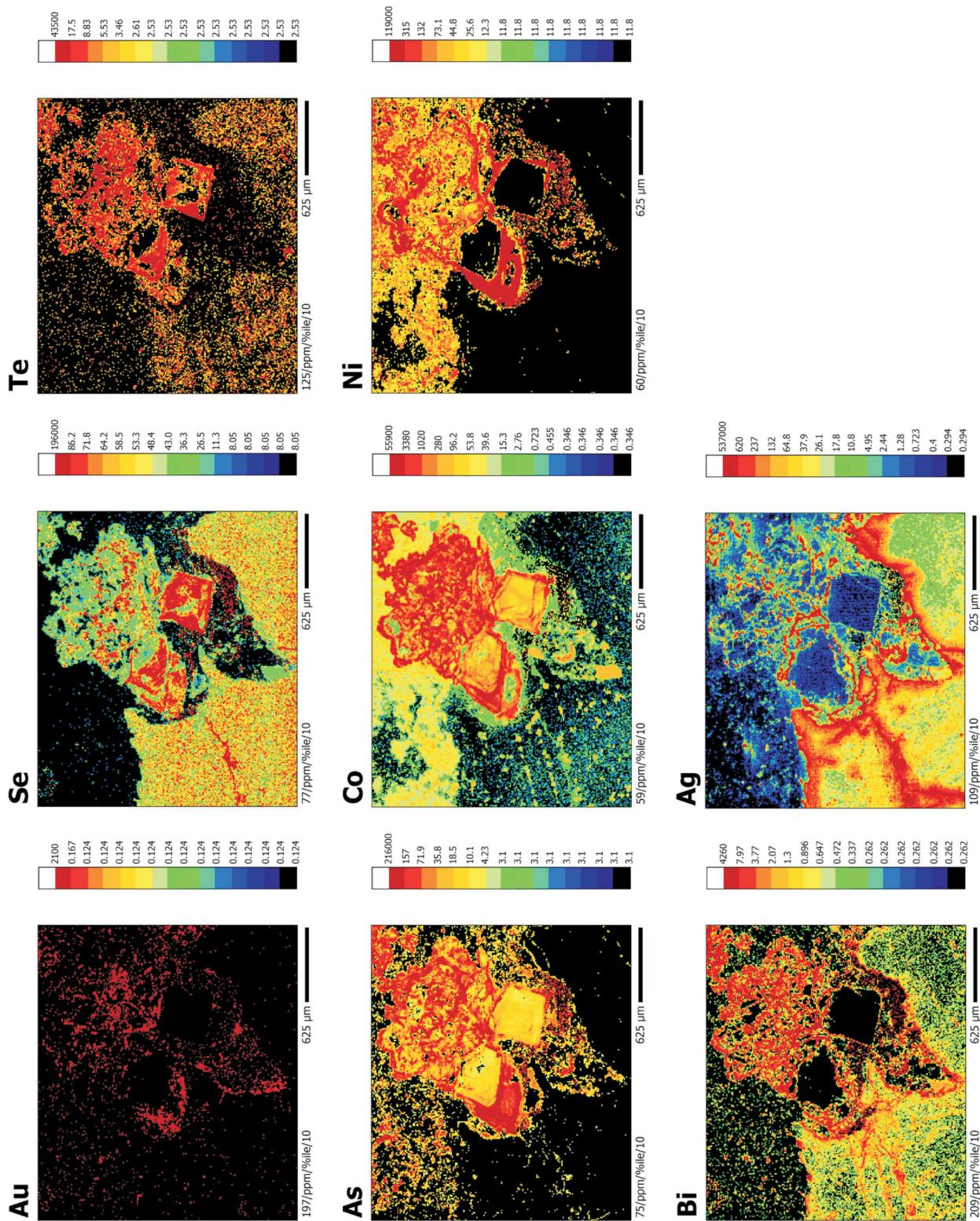
Figure 6. LA-ICP-MS trace-element maps of ^{197}Au, ^{77}Se, ^{125}Te, ^{75}As, ^{59}Co, ^{60}Ni, ^{209}Bi, and ^{109}Ag in sulphide minerals from sample 212.7. Concentrations are in ppm.

higher concentrations of Co, Bi, Te, As and Ag, with sample 212.4 additionally containing Pt in these zones.

Both Au and Ag mineralization appears to have been concentrated late in the hydrothermal evolution of the deposit. This is evident from the spatial trends in the trace-element maps, where both elements are absent from the innermost regions of pyrite and chalcopyrite. Instead, they are found primarily in late rims of pyrite or chalcopyrite grains, along fractures through grains or in the matrix between grains. Gold is absent from coarse crystalline pyrite cores in each sample but does occur within rim domains and as micro-inclusions associated with fractures, consistent with it entering the system prior to the latest fracture mineralization.

At the resolution of the analyses, Ag in chalcopyrite appears to occur in solid solution rather than as micro-inclusions. This is reflected by the broad, semicontinuous zones of Ag enrichment in chalcopyrite near grain boundaries and bordering fractures. These textures may indicate late replacement or reprecipitation reactions within chalcopyrite due to late Ag-rich fluids travelling through the system, resulting in the incorporation of Ag into the chalcopyrite crystal lattice.

Separation of quantitative data corresponding to pyrite mineralization through principal-component analysis allowed for further interpretations to be made. As shown in Figure 7, various plots of elements in pyrite can inform the conditions and processes behind mineralization, such as Co and Ni ratios. The Co and Ni ratios have been used to identify the processes responsible for pyrite mineralization, with Co/Ni >1 indicating hydrothermal processes, Co/Ni <1 indicating sedimentary processes and pyrite of volcanogenic origin having Co/Ni values between 5 and 50 (Bajwah et al., 1987). Pyrite formed from magmatic processes is characterized by high concentrations of Ni and Co compared to pyrite from other processes (Bajwah et al., 1987). However, the vast majority of pyrite analyses included as part of the current study yield lower Ni and Co concentrations that are more typical of volcanic and hydrothermal pyrite (Figure 7a). A smaller number of analyses yielded Ni and Co concentrations that are similar to those in pyrite of magmatic and sedimentary origin (Figure 7a). The pyrite cores in all three samples yield compositions that are most similar to volcanogenic pyrite (Figure 7a). Pyrite rims from samples 138.4 and 212.7 display Co-poor sedimentary characteristics, resulting in Co/Ni values below 1, and plot within the sedimentary field (Figure 7a). The latest pyrite rims in sample 212.7 plot primarily in the hydrothermal (above Co/Ni = 1 line) and volcanogenic (above Co/Ni = 10 line) fields (Figure 7a).

Trends of Ag/Co vs. Co/Cu recorded in pyrite have been used as a relative thermometer to differentiate distal low-temperature zones from proximal high-temperature zones associated with high-grade mineralization in the core of porphyry deposits (Rivas-Romero et al., 2021). The material analyzed from all three samples generally overlaps the same range of temperature (Figure 7b), with the exception of pyrite-rim domains from sample 212.7 that are consistent with higher temperature pyrite mineralization. The pyrite rims that crystallized at higher apparent temperature may reflect infiltration of high-temperature hydrothermal fluid that accompanied the late mineralization event responsible for the crystallization of pyrite rims. Values of Co/Ni from the same domains plot primarily within the hydrothermal zone (Figure 7a), consistent with such an origin.

Relative Au solubility in pyrite can be visualized in As versus Au plots (Figure 7c). Above the line, Au is expected to occur as inclusions, whereas, below the line, Au may occur in solid solution (Reich et al., 2005). In pyrite, As can substitute for S within the pyrite lattice during periods of rapid pyrite precipitation (Abraitis et al., 2004). Zones with increased As concentration in pyrite are associated with higher concentrations of trace elements because As is typically incorporated into the pyrite lattice through coupled substitution (Abraitis et al., 2004; Lin et al., 2023). Gold is one element that is incorporated into the pyrite lattice through coupled substitution with As, which results in a positive correlation within pyrite (Abraitis et al., 2004; Lin et al., 2023). According to the plot in Figure 7c, the Au that occurs in late pyrite-rim domains, as opposed to fracture-infilling Au, is present primarily in solid solution rather than in inclusions. Although there is an overlap of As- and Au-rich zones in the three samples analyzed in this study, the appearance of Au within pyrite also displays a nugget-like texture (Figures 4, 5, 6, 7c). If Au was being incorporated into pyrite through solid solution, then more gradual homogeneous textures would be expected in the trace-element maps. The nugget-like texture and the As/Au plot indicate that Au is occurring in pyrite as both solid solution and inclusions. Regardless of texture, Au is associated with late pyrite rims and also within the surrounding matrix, indicating that Au mineralization occurred late in the hydrothermal evolution of the system.

The characteristics of the trace-element maps and discrimination plots are consistent with a depleted late-magmatic or post-emplacement hydrothermal event that resulted in the mineralization of pyrite cores depleted in Bi, Te, Co, Ni and Au. Later periods of hydrothermal activity appear to have introduced fluids enriched in Au and critical elements Bi, Te, Co and Ni. Consequently, as pyrite mineralized from these enriched fluids, Bi, Te, Co, Ni and Au were incorporated into rim domains, which the Ni/Co plot also indicates are hydrothermal in origin. The Ag/Co vs. Co/Cu plot indicates that late pyrite-rim mineralization occurred in a high-temperature environment with initial mineralization of Au; later accumulation followed in fractures within pyrite
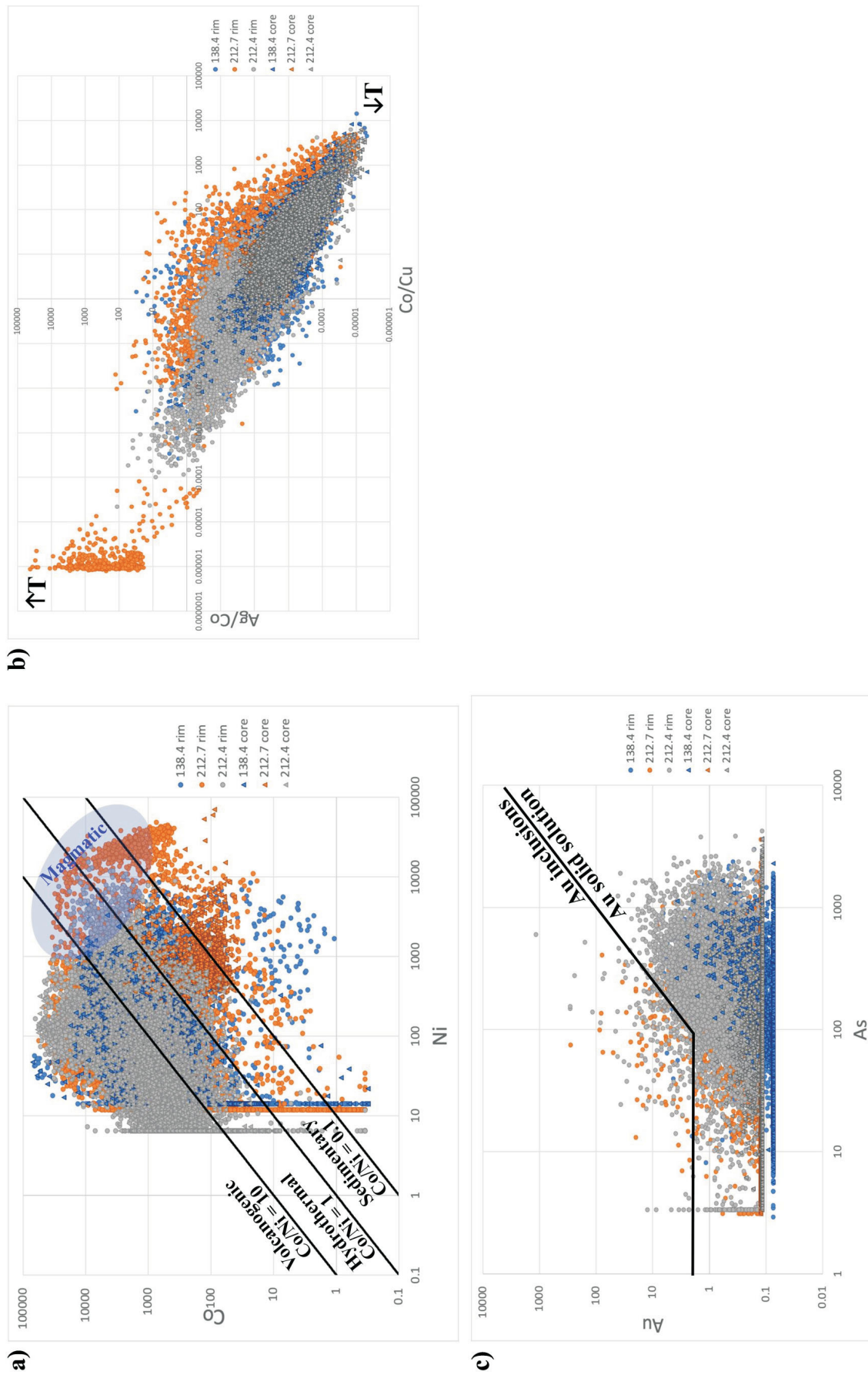
Figure 7. Scatterplots comparing trace-element concentrations in pyrite from samples 138.4 (blue), 212.7 (orange), and 212.4 (grey): **a)** Ni vs. Co to determine pyrite origin, the light blue ellipse indicating a magmatic origin; **b)** Co/Cu vs. Ag/Co plot showing temperature of mineralization; and **c)** As vs. Ag plot to determine gold solubility in pyrite.

grains and the surrounding matrix. The late fluids also interacted with chalcopyrite within the system, resulting in the incorporation of Ag through either replacement or reprecipitation reactions along chalcopyrite-crystal boundaries and fractures.

Preliminary Observations

Through trace-element mapping, interpretations have been made regarding the occurrence and abundance of Au, Ag and critical minerals of Bi, Te, Co, and Ni, and the processes that formed mineralization within the Burgundy Ridge prospect. Qualitative and quantitative data from trace-element mapping of sulphides have demonstrated the presence of

- multiple generations of mineralization;
- pyrite cores that have been depleted, and rims that have been enriched, with respect to critical minerals;
- late Ag and Au mineralization; and
- formation of pyrite due to hydrothermal and volcanogenic processes.

Overall, these data provide a detailed initial understanding of sulphide paragenesis within the deposit, with late high-temperature hydrothermal fluids forming the majority of mineralization within the Burgundy Ridge prospect.

Future Work

The trace-element map data will be combined with in situ sulphur isotope and Rb-Sr geochronology analysis to support current preliminary observations. In situ Rb-Sr geochronology of mica cogenetic with sulphides in the system will be used to determine the timing of mineralization for the Burgundy Ridge prospect. Interpretations from in situ sulphur isotope analysis of chalcopyrite and pyrite from multiple samples throughout the deposit will be used to further determine the conditions of hydrothermal fluids relating to mineralization, such as temperature and pH. Through the Geological Survey of Canada's Targeted Geoscience Initiative, the findings from this study will be combined with other research on silica-undersaturated alkalic porphyry deposits in BC, such as Galore Creek. This will contribute to the overall understanding of these deposit types, which host economically significant amounts of critical minerals and other minerals, such as gold.

Acknowledgments

References

Abraitis, P.K., Pattrick, R.A.D. and Vaughan, D.J. (2004): Variations in the compositional, textural and electrical properties of natural pyrite: a review; International Journal of Mineral Processing, v. 74, p. 41–59.

Bajwah, Z.U., Seccombe, P.K. and Offler, R. (1987) Trace element distribution, Co:Ni ratios and genesis of the Big Cadia iron-copper deposit, New South Wales, Australia; Mineralium Deposita, v. 22, p. 292–300.

BC Geological Survey (2015): Gold in British Columbia; BC Ministry of Energy, Mines and Low Carbon Innovation, BC Geological Survey, Information Circular 2015-06, URL <https://www2.gov.bc.ca/assets/gov/farming-natural-resources-and-industry/mineral-exploration-mining/documents/mineral-development-office/gold_september_2015.pdf> [October 2023].

BC Geological Survey (2018): The Golden Triangle of northwestern British Columbia; BC Ministry of Energy, Mines and Low Carbon Innovation, BC Geological Survey, Information Circular 2018-05, URL <https://cmscontent.nrs.gov.bc.ca/geoscience/publicationcatalogue/InformationCircular/BCGS_IC2018-05.pdf> [October 2023].

Cabri, L. and Jackson, S. (2011): New developments in characterization of sulfide refractory Au ores; World Gold 2011, 50th Conference of Metallurgists. MetSoc, October 2–5, Montreal, Quebec, p. 51–62.

Coney, P.J., Jones, D.L. and Monger, J.W.H. (1980): Cordilleran suspect terranes; Nature, v. 288, p. 329–333.

del Real, I., Hart, C.J.R., Bouzari, F., Blackwell, J.L., Rainbow, A., Sherlock, R. and Skinner, T. (2013): Paragenesis and alteration of the Southeast Zone and Deerhorn porphyry deposits, Woodjam property, central British Columbia (parts of 093A); in Geoscience BC Summary of Activities 2012, Geoscience BC, Report 2013-1, p. 79–90, URL <https://cdn.geosciencebc.com/pdf/SummaryofActivities2013/SoA2013_delReal.pdf > [November 2023].

Deyell, C. L. and Tosdal, R. M. (2005): Alkalic Cu-Au deposits of British Columbia: sulfur isotope zonation as a guide to mineral exploration; in Geological Fieldwork 2004, BC Ministry of Energy, Mines and Low Carbon Innovation, BC Geological Survey, Paper 2005-1, p. 191–208, URL <https://www.researchgate.net/publication/255586554_Alkalic_Cu-Au_Deposits_of_British_Columbia_Sulfur_Isotope_Zonation_as_a_Guide_to_Mineral_Exploration> [October 2023].

Dickinson, W.R. (2004): Evolution of the North American Cordillera; Annual Review of Earth and Planetary Sciences, v. 32, p. 13–45.

Enduro Metals Corp. (2022): Newmont Lake: our flagship project in British Columbia's Golden Triangle; Enduro Metals Corp., website, URL <https://endurometals.com/newmont-lake/> [October 2023].

Enduro Metals Corp. (2023): Enduro outlines 20 km structural corridor controlling copper-gold mineralization at Newmont Lake; Enduro Metals Corp., press release, May 24, 2023, URL <https://endurometals.com/enduro-outlines-20km-structural-corridor-controlling-copper-gold-mineralization-at-newmont-lake/> [October 2023].

Government of Canada (2022): The Canadian Critical Minerals Strategy; Government of Canada, online document, <https://www.canada.ca/content/dam/nrcan-rncan/site/critical-minerals/Critical-minerals-strategyDec09.pdf> [October 2023].

Guillong, M., Hametner, K., Reusser, E., Wilson, S.A. and Günther, D. (2005): Preliminary characterisation of new glass reference materials (GSA-1G, GSC-1G, GSD-1G and GSE-1G) by laser ablation–inductively coupled plasma–mass spectrometry using 193 nm, 213 nm and 266 nm wavelengths; Geostandards and Geoanalytical Research, v. 29, p. 315–331, URL <https://onlinelibrary.wiley.com/doi/abs/10.1111/j.1751-908X.2005.tb00903.x> [November 2023].

Jackson, S. (2008): LAMTRACE data reduction software for LA-ICP-MS; in Laser Ablation ICP-MS in the Earth Sciences: Current Practices and Outstanding Issues, P. Sylvestor (ed.), Mineralogical Association of Canada, Short Course Series, v. 40, p. 305–307.

Lang, J.R., Lueck, B., Mortensen, J.K., Kelly Russell, J., Stanley, C.R. and Thompson, J.F.H. (1995): Triassic-Jurassic silica-undersaturated and silica-saturated alkalic intrusions in the Cordillera of British Columbia: implications for arc magmatism; Geology, v. 23, p. 451–454.

Lawley, C.J.M., Petts, D.C., Jackson, S.E., Zagorevski, A., Pearson, D.G., Kjarsgaard, B.A., Savard, D. and Tschirhart, V. (2020) Precious metal mobility during serpentinization and breakdown of base metal sulphide; Lithos, v. 354–355, URL <https://doi.org/10.1016/j.lithos.2019.105278>.

Lin, S., Hu, K., Cao, J., Liu, Y., Liu, S. and Zhang, B. (2023): Coupling and decoupling of Au and As in pyrite from Carlin-type Au deposits, southwest China; Journal of Asian Earth Sciences, v. 246, URL <https://doi.org/10.1016/j.jseaes.2023.105582>.

Logan, J.M. and Mihalynuk, M.G. (2014): Tectonic controls on Early Mesozoic paired alkaline porphyry deposit belts (Cu-Au ± Ag-Pt-Pd-Mo) within the Canadian Cordillera; Economic Geology, v. 109, no. 4, p. 827–858, URL <https://doi.org/10.2113/econgeo.109.4.827>.

Micko, J. (2010): The geology and genesis of the Central Zone alkalic copper-gold porphyry deposit, Calgore Creek district, northwestern British Columbia, Canada; Ph.D. thesis, The University of British Columbia, 359 p.

Monger, J.W.H. and Gibson, H.D. (2019): Mesozoic-Cenozoic deformation in the Canadian Cordillera: the record of a "Continental Bulldozer"?; Tectonophysics, v. 757, p. 153–169, URL <https://doi.org/10.1016/j.tecto.2018.12.023>.

Nelson, J. and Colpron, M. (2007): Tectonics and metallogeny of the British Columbia, Yukon and Alaskan Cordillera, 1.8 Ga to the present; in Mineral Deposits of Canada: A Synthesis of Major Deposit-Types, District Metallogeny, the Evolution of Geological Provinces, and Exploration Methods; W.D. Goodfellow (ed.), Geological Association of Canada, Mineral Deposits Division, Special Publication No. 5, p. 755–791.

Ray, G.E., Jaramillo, V.A. and Ettlinger, A.D. (1990): The McLymont northwest zone, northwestern British Columbia: a gold-rich retrograde skarn? (104B); in Geological Fieldwork 1990, BC Ministry of Energy, Mines and Low Carbon Innovation, BC Geological Survey, Paper 1991-1, p. 255–262, URL <https://citeseerx.ist.psu.edu/document?repid=rep1&type=pdf&doi=efa214a1887c945e4e40f25f20f5c27b6459030e> [October 2023].

R Development Core Team (2018): R: a language and environment for statistical computing; R Foundation for Statistical Computing, Vienna, Austria, URL <https://www.R-project.org> [October 2023].

Reich, M., Kesler, S.E., Utsunomiya, S., Palenik, C.S., Chryssoulis, S.L. and Ewing, R.C. (2005): Solubility of gold in arsenian pyrite; Geochimica et Cosmochimica Acta, v. 69, no. 11, p. 2781–2796 URL <https://doi.org/10.1016/j.gca.2005.01.011>.

Rivas-Romero, C., Reich, M., Barra, F., Gregory, D. and Pichott, S. (2021): The relation between trace element composition of Cu-(Fe) sulfides and hydrothermal alteration in a porphyry copper deposit: insights from the Chuquicamata underground mine, Chile; Minerals, v. 11, p. 1–29, URL <https://doi.org/10.3390/min11070671>.

Templ, M., Hron, K. and Filzmoser, P. (2011): robCompositions: an R-package for robust statistical analysis of compositional data; in Compositional Data Analysis: Theory and Applications. V. Pawlowsky-Glahn and A. Buccianti, A. (ed.), John Wiley & Sons, Ltd, Chichester, UK, p. 341–355, URL <DOI:10.1002/9781119976462>.

Tombe, S.P. (2020): Exploration and mining in the northwest region, British Columbia; provincial overview of exploration and mining in British Columbia, 2019; BC Ministry of Energy, Mines and Low Carbon Innovation, BC Geological Survey, Information Circular 2020-01, p. 41–58.